PERGAMON

International Journal of Heat and Mass Transfer 44 (2001) 4725–4736

International Journal of HEAT and MASS TRANSFER

www.elsevier.com/locate/ijhmt

A study of buoyancy-driven flow in a confined fluid overlying a porous layer

J.J. Valencia-López, J.A. Ochoa-Tapia *

Departamento de Ingeniería de Procesos e Hidráulica, Unidad Iztapalapa, Universidad Autónoma Metropolitana, Av. Michoacán y La Purísima s/n, Col. Vicentina CP 09340, México, DF, Mexico

Received 16 December 1999; received in revised form 12 September 2000

Abstract

Two different models to analyze the natural convection in a confined fluid overlying a porous media were compared. The first approach used the Navier–Stokes equation and Darcy's law coupled by Beavers and Joseph (B–J) interfacial boundary condition. Instead, the second approach considered the Brinkman extended Darcy's law together with the continuity of stress and velocity in the fluid/porous medium dividing surface. The numerical predictions were mainly used to analyze the effects of the Rayleigh and Darcy numbers on the local and average Nusselt numbers of the cold and hot walls. Significant differences between the overall average Nusselt numbers were found when the Rayleigh and Darcy numbers were large enough.

1. Introduction

A thorough understanding of the physics of buoyancy-driven flows in fluids overlying porous media is essential when designing thermal insulation systems, grain stores in which poisonous gases such as phosphine are used to kill insect pests, thermal energy storage systems. On a more fundamental level, such systems demand attention because there remain unsolved problems regarding the momentum boundary conditions at the interface of the fluid and porous layers. For example, a little-addressed issue concerns the validity of the assumption of local thermodynamic equilibrium between the interstitial fluid and the solid phase [1].

Several studies of buoyancy-driven flows in two-dimensional fluid/porous systems have been reported, i.e., [2–7]. Singh et al. [8] have presented a numerical study of three-dimensional natural convection in a confined fluid overlying a porous layer using the Brinkman-extended Darcy's formulation. In the works reported above, the authors generally used one of two approaches to define the momentum boundary conditions at the fluid/porous medium interface. Most frequently it is the approach that involves Brinkman's [9] "correction" to Darcy's law that is deemed to apply in the porous layer, that has been used. In this case, the differential equations that govern the momentum transport in both the fluid and porous layers are rendered in the same order so that it is possible to match the rates of strain in both regions. In many cases, when Brinkman's [8] correction is used, the effective viscosity of the porous layer is introduced as an empirical parameter. Recently, Ochoa-Tapia and Whitaker [10] derived a stress jump condition to couple Navier–Stokes equation and Darcy's equation with the Brinkman's correction, and it was found there is not theoretical reason to use the effective viscosity as an empirical parameter.

A second method to match the momentum equations at the fluid/porous medium inter-region is to make use of an empirical expression proposed by Beavers and Joseph (B–J) [11]. This expression relates the rate of strain in the fluid phase to the difference between the tangential velocities in the fluid and porous layers adjacent to the inter region. The B–J boundary condition also requires the determination of an empirical parameter. One reason for the difficulty in properly defining the momentum boundary condition at the fluid/porous

* Corresponding author. Tel.: +52-5804-46-48; fax: +52-5804-49-00.

E-mail address: jaot@xanum.uam.mx (J.A. Ochoa-Tapia).

0017-9310/01/$ - see front matter
PII: S0017-9310(01)00105-3

Nomenclature

Da	Darcy number ($P_{\gamma\omega}/L_x^2$)
$\mathbf{i}, \mathbf{j}, \mathbf{k}$	Cartesian unit vectors
K_ω	dimensionless porous media/fluid conductivity ratio
L_x	length of the container in the x direction (m)
$p_{\gamma\omega}$	permeability of fluid γ in porous media ω (m^2)
Pr	Prandtl number (ν_γ/α_γ)
p_γ	dimensionless pressure
Ra	Rayleigh number for the porous media ($g\beta_\gamma(T_h - T_c)L_x^3/(\alpha_\gamma\nu_\gamma)$)
T	temperature (K)
$\mathbf{v}_\lambda$	dimensionless velocity vector in the λ region
X, Y, Z	dimensionless Cartesian coordinates (x/L_x, y/L_x, z/L_x)

Greek symbols

α	Beavers and Joseph boundary condition parameter (dimensionless)
α_γ	thermal diffusivity of fluid ($m^2\ s^{-1}$)
ζ_λ	dimensionless vorticity vector
$\zeta_{X\lambda}$	X component of the dimensionless vorticity vector in the λ region
θ_λ	dimensionless temperature in the λ region
μ_γ	viscosity of fluid (kg $m^{-1}\ s^{-1}$)
ν_γ	viscous diffusivity of fluid ($m^2\ s^{-1}$)
$\mathbf{\Psi}_\lambda$	dimensionless vector potential
$\Psi_{X\lambda}$	X component of the dimensionless vector potential in the λ region
$\langle\psi_\gamma\rangle_\lambda$	superficial average of the ψ_γ variable in region λ
$\langle\psi_\gamma\rangle_\lambda^\gamma$	intrinsic average of the ψ_γ variable in region λ

Subscripts

c	cold wall
h	hot wall
γ	fluid
η	clear fluid region
λ	η or ω
ω	porous medium region

layer interface may be the inadequate definitions of volume-averaged quantities in this region (see, for example, [1]).

The objective in this work is to use the B–J [11] boundary condition to analyze the natural convection in a three-dimensional enclosure containing a fluid and a porous medium. The numerical predictions are compared with the results obtained from the solution that uses the Brinkman correction factor [8].

2. Theory

2.1. Governing differential equations

The system is formed by a fluid (γ-phase) and a granular material (σ-phase) distributed in two layers (Fig. 1). The upper layer is a clear fluid and the lower layer is a porous media formed by the two phases. To avoid the complexity of dealing with the geometric details of the porous medium, we model the natural convection process in terms of average transport equations valid in the porous medium (region ω) and the homogeneous fluid (region η). The average transport equations for the clear fluid region have the same form that the point transport equations as long as some length constraints are satisfied [10]. The x-axis is the direction of gravity, while the y- and z-axes are in the horizontal plane. The Boussinesq approximation is imposed: physical properties are constants, but density is in the body force term. Also, the analysis is restricted to isotropic heat and momentum transport in the porous region.

In this work, Darcy's law is used to represent the momentum transport in the porous medium. In this expression we have not included the inertial terms as suggested by the theoretical development of Whitaker [12]. Under these considerations the dimensionless governing differential equations are the following:

Porous layer (ω-region):

Continuity equation

$$\nabla \cdot \mathbf{v}_\omega = 0. \tag{1}$$

Darcy's equation

$$\mathbf{v}_\omega = -Da\nabla p_\gamma + Da\,Ra\theta_\omega \mathbf{i}. \tag{2}$$

One-equation model for energy

$$\nabla \cdot (\mathbf{v}_\omega \theta_\omega) = K_\omega \nabla^2 \theta_\omega. \tag{3}$$

Homogeneous fluid (η-region):

Continuity equation

$$\nabla \cdot \mathbf{v}_\eta = 0. \tag{4}$$

Navier–Stokes equation

$$\nabla \cdot (\mathbf{v}_\eta \mathbf{v}_\eta) = -Pr\nabla p_\eta + Pr\nabla^2 \mathbf{v}_\eta + PrRa\ \theta_\eta \mathbf{i}. \tag{5}$$

Energy-equation

$$\nabla \cdot (\mathbf{v}_\eta \theta_\eta) = \nabla^2 \theta_\eta. \tag{6}$$

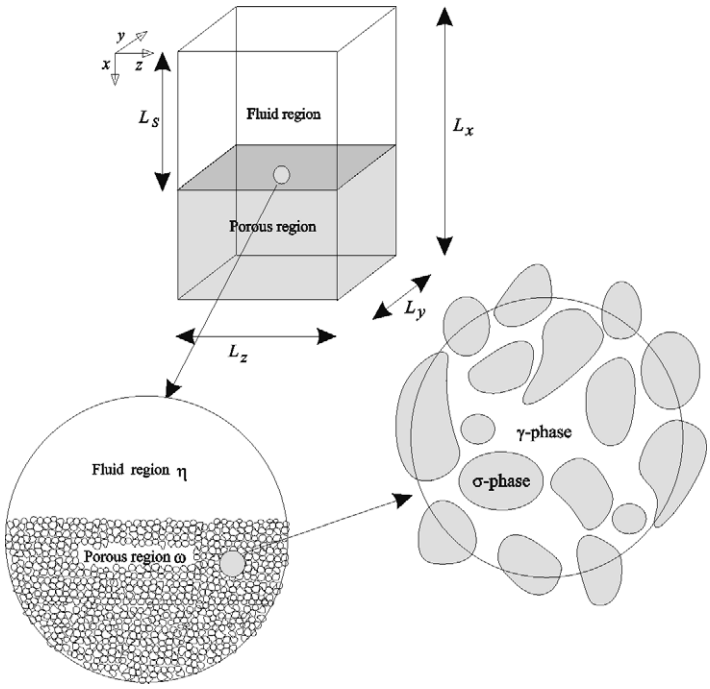

Fig. 1. System under analysis, porous region details and coordinate system.

The dimensionless velocity vector, temperature and pressure variables introduced in Eqs. (1)–(6) are:

$$\mathbf{v}_\lambda = \frac{\left\langle \mathbf{v}'_\gamma \right\rangle_\lambda}{\alpha_\gamma / L_x}, \quad \theta_\lambda = \frac{\langle T_\gamma \rangle_\lambda - T_\mathrm{h}}{T_\mathrm{h} - T_\mathrm{c}}, \quad p_\lambda = \frac{\langle p_\gamma \rangle_\lambda^\gamma}{\mu_\gamma \alpha_\gamma / L_x^2}. \tag{7}$$

Here $\langle \mathbf{v}'_\gamma \rangle_\lambda$ is the superficial average of the fluid dimensional velocity, and the subscript λ indicates the ω-region or the η-region. The characteristic length L_x is the height of the system. T_h and T_c indicate the temperatures at which the hot ($Y = 0$) and cold ($Y = L_y/L_x$) walls are kept. Also, we have used the thermal diffusivity α_γ and viscosity of the fluid μ_γ to define the characteristic velocity and pressure.

In Eq. (7) the symbols $\langle \psi_\gamma \rangle_\lambda$ and $\langle \psi_\gamma \rangle_\lambda^\gamma$ represent the superficial average and the intrinsic phase average of the point variables ψ_γ, respectively [13]. In the derivation of Eq. (3), the thermal equilibrium principle was invoked [1]. Therefore, one temperature is used as a reasonable approximation for the average temperatures of both phases in the homogeneous porous region: $\langle T \rangle_\omega = \langle T_\gamma \rangle_\omega^\gamma = \langle T_\sigma \rangle_\omega^\sigma$. In Eq. (3), K_ω is the dimensionless effective conductivity in the porous medium.

The Darcy, Rayleigh and Prandtl numbers are defined by:

$$Da = \frac{P_{\gamma\omega}}{L_x^2}, \quad Ra = \frac{g\beta_\gamma (T_\mathrm{h} - T_\mathrm{c}) L_x^3}{\alpha_\gamma \nu_\gamma}, \quad Pr = \frac{\nu_\gamma}{\alpha_\gamma}. \tag{8}$$

2.2. Boundary conditions

For the velocity, non-slip and no penetration boundary conditions were imposed at the container walls. For the energy equation the vertical walls at $Y = 0$ and $Y = L_y/L_x$ were kept at T_h and T_c, respectively. In the other four walls non-zero flux boundary conditions were imposed.

For the inter-region between the clear fluid and the porous medium located at $X = X_s$, the following conditions for temperature and velocity were used:

$$\theta_\omega = \theta_\eta, \tag{9}$$

$$-\mathbf{n}_{\omega\eta} \cdot K_\omega \nabla \theta_\omega = -\mathbf{n}_{\omega\eta} \cdot \nabla \theta_\eta, \tag{10}$$

$$-\mathbf{n}_{\omega\gamma} \cdot \mathbf{v}_\omega = -\mathbf{n}_{\omega\gamma} \cdot \mathbf{v}_\eta, \tag{11}$$

$$-\mathbf{t}_{\omega\eta} \cdot \frac{\partial \mathbf{v}_\omega}{\partial X} = \frac{\alpha}{\sqrt{Da}} \mathbf{t}_{\omega\eta} \cdot (\mathbf{v}_\omega - \mathbf{v}_\eta) \quad \text{for } \mathbf{t}_{\omega\eta} = \mathbf{j}, \mathbf{k}. \tag{12}$$

In Eqs. (10) and (11) $\mathbf{n}_{\omega\eta}$ is the unit normal vector at the dividing surface between the porous and the clear fluid directed from the ω-region to the η-region. In Eq. (12), that is an extension of the semi empirical B–J boundary condition for momentum, α is the B–J parameter, and the tangent unit vectors (**j** or **k**) are indicated by $\mathbf{t}_{\omega\eta}$.

Other authors have solved the same problem using Brinkman-extended Darcy's formulation [8]. The main difference of the Brinkman-extended Darcy's model with respect to the formulation presented in this work is the inclusion of Brinkman's term in Eq. (2). This adds a velocity Laplacian term in the momentum equation that

enables the use of the continuity of stress tensor and velocity in the interfacial region. Also, with this formulation, non-slip boundary conditions can be applied easily at the container wall in contact with the porous medium.

2.3. Vorticity–potential vector formulation

To avoid the solution of the problem defined in terms of primitive variables, by Eqs. (1)–(6) subjected to the boundary conditions Eqs. (9)–(12), we used the vorticity–vector potential approach [14,15]. The relationships between velocity with vorticity and the potential are:

$$\zeta_\lambda = \nabla \times \mathbf{v}_\lambda \quad \text{for } \lambda = \omega, \eta, \tag{13}$$

$$\mathbf{v}_\lambda = \nabla \times \boldsymbol{\Psi}_\lambda \quad \text{for } \lambda = \omega, \eta. \tag{14}$$

Introducing Eqs. (13) and (14) into the momentum transport and the continuity equations along with some manipulation yields the new formulation for the momentum transport problem:

Porous layer (ω-region):

$$\nabla^2 \boldsymbol{\Psi}_\omega = -\zeta_\omega, \tag{15}$$

$$-\zeta_\omega + Da\,Ra \nabla \times (\mathbf{i}\theta_\omega) = 0. \tag{16}$$

Fluid layer (η-region):

$$\nabla^2 \boldsymbol{\Psi}_\eta = -\zeta_\eta, \tag{17}$$

$$\mathbf{v}_\eta \cdot \nabla \zeta_\eta - \zeta_\eta \cdot \nabla \mathbf{v}_\eta = Pr \nabla^2 \zeta_\eta + RaPr \nabla \times (\theta_\eta \mathbf{i}). \tag{18}$$

It should be noted that it is not necessary to solve a vector vorticity differential equation in the porous media region. In the approach followed in this work the vorticity was evaluated with Eq. (16) using the temperature field data available.

2.4. Boundary conditions for vorticity

For the boundary condition for each component of the vector ζ_λ at the container walls we followed the work of Mallinson and de Vahl Davis [16]:

$$\zeta_n = 0, \quad \zeta_{t_1} = -\frac{\partial^2 \Psi_{t_1}}{\partial n^2}, \quad \zeta_{t_2} = -\frac{\partial^2 \Psi_{t_2}}{\partial n^2}. \tag{19}$$

Here n indicates the normal Cartesian coordinate at the wall (the Cartesian coordinate that is kept constant at the surface) and t_1 and t_2 are the other two coordinates. The vorticity components for the clear fluid at the plane located at $X = X_s$ were evaluated from the following expressions derived from the normal velocity continuity condition and the B–J boundary conditions, Eqs. (11) and (12):

$$\zeta_{X\eta} = \left(\frac{\partial \Psi_z}{\partial Y} - \frac{\partial \Psi_y}{\partial Z}\right)_\omega - \left(\frac{\partial \Psi_z}{\partial Y} - \frac{\partial \Psi_y}{\partial Z}\right)_\eta + \left(\frac{\partial w}{\partial Y} - \frac{\partial v}{\partial Z}\right)_\eta, \tag{20}$$

$$\zeta_{Y\eta} = \frac{\alpha}{\sqrt{Da}}\left[\left(\frac{\partial \Psi_Y}{\partial X} - \frac{\partial \Psi_X}{\partial Y}\right)_\eta - \left(\frac{\partial \Psi_Y}{\partial X} - \frac{\partial \Psi_X}{\partial Y}\right)_\omega\right] + \frac{\partial u_\eta}{\partial Z}, \tag{21}$$

$$\zeta_{Z\eta} = -\frac{\alpha}{\sqrt{Da}}\left[\left(\frac{\partial \Psi_X}{\partial Z} - \frac{\partial \Psi_Z}{\partial X}\right)_\eta - \left(\frac{\partial \Psi_X}{\partial Z} - \frac{\partial \Psi_Z}{\partial X}\right)_\omega\right] - \frac{\partial u_\eta}{\partial Y}. \tag{22}$$

2.5. Boundary conditions for the vector potential

To enforce no fluid penetration at the container walls, the boundary conditions for each component of the vector $\boldsymbol{\Psi}_\lambda$ were chosen as follows:

$$\frac{\partial \Psi_n}{\partial n} = 0 \quad \text{and} \quad \Psi_{t_1} = \Psi_{t_2} = 0. \tag{23}$$

The interfacial boundary conditions at the plane $X = X_s$ where imposed through the solution of Eqs. (15) and (13) at the interfacial surface using the corresponding value of the vorticity.

2.6. Nusselt number

From the practical point of view, it is interesting to evaluate the heat transfer rate resulting from the temperature difference between the hot and cold walls. In this work the heat transfer effects are reported in terms of the following average Nusselt number at the cold and hot walls:

Width average Nusselt number

$$\overline{Nu}_X(X)\,|_{Y^*} = \frac{L_X}{L_Z}\int_0^{L_Z/L_X} Nu(X,Z)\,|_{Y^*}\,\mathrm{d}Z. \tag{24a}$$

Overall average Nusselt number

$$\overline{Nu}\,|_{Y^*} = \frac{L_X}{L_Z}\int_0^1 \int_0^{L_Z/L_X} Nu(X,Z)\,|_{Y^*}\,\mathrm{d}Z\,\mathrm{d}X. \tag{24b}$$

In Eqs. (24a) and (24b) the subscript Y^* indicates evaluation at $Y = 0$ or $Y = L_Y/L_X$, and $Nu(X,Z)$ is the local Nusselt number at the cold or hot walls given by:

$$Nu(X,Z) = \frac{hL_X}{k_\gamma} = \begin{cases} -\dfrac{\partial \theta_\eta}{\partial Y}, & \text{for } 0 \leqslant X < X_s, \\ -\dfrac{1}{2}\left(\dfrac{\partial \theta_\eta}{\partial Y} + K_\omega \dfrac{\partial \theta_\omega}{\partial Y}\right), & \text{at } X = X_s, \\ -K_\omega \dfrac{\partial \theta_\omega}{\partial Y}, & \text{for } X_s < X \leqslant 1. \end{cases} \tag{25}$$

3. Numerical solution

The nonlinear system of governing differential equations of the vector potential, the vorticity vector and the

temperature was solved using a procedure similar to that presented by Mallinson and de Vahl Davis [14] for natural convective flows of single-phase fluids. In that method, the differential equations are transformed into parabolic form by adding false transient terms and then represented in finite difference form. The discretized equations are then iterated, until steady state, using the alternating direction implicit (ADI) method proposed by Peaceman and Rachford [17]. The described procedure allows the decoupling of the differential equations if information of previous iterations is used. Therefore, initial values of the fields are needed and different sequences can be attempted to solve the problem.

3.1. The solution of the model that involves the B–J interfacial boundary condition

For the solution of this model, the equations were solved in the following order.

(a) The temperature field was obtained by solving Eqs. (3) and (6). The first ADI march was in the vertical direction, it started one node after $X = 0$ and it finished one node before $X = 1$. The interfacial node at $X = X_s$ was not included in this sweep. When required, the previous iteration values of the temperature at the walls and $X = X_s$ were used. Afterwards the marching in the Y and Z directions were performed. Finally, the temperature fields at X_s and the wall container were updated using Eqs. (9) and (10) and the adiabatic wall conditions.

(b) The components of the vorticity vector for the clear fluid region were obtained by solving Eq. (18) using the temperature and velocity fields obtained in the previous iteration. In this case, the values for the vorticity components obtained from Eqs. (20) and (21), using values of the potential vectors from the previous iteration, were used as boundary conditions at X_s. Therefore, the ADI march in the X direction was similar to the one described above for temperature. The vorticity vector field for the porous medium region was updated by direct calculation from Eq. (16), and using the temperature field from the previous iteration.

(c) The vector potential components for the upper region were obtained from the solution of Eq. (17) using a similar ADI procedure. For the X direction march, the boundary condition at X_s was not imposed directly. Instead, the governing differential equation was discretized using backward Taylor series expansion in $X = X_s$.

A similar procedure, but using forward Taylor series expansion at $X = X_s$, was used for the solution of Eq. (15) to update the porous medium fields of the vector potential components.

The iteration procedure was repeated as many times as needed to satisfy the convergence criterion that was established for each one of the variables following Mallinson and de Vahl Davis [14]:

$$\frac{1}{M_X M_Y M_Z}\sum_{i=1}^{i=M_X}\sum_{j=1}^{j=M_Y}\sum_{k=1}^{k=M_Z}\frac{|\Delta\varphi_{ijk}^N|}{|\varphi_{\max}^N|} \leqslant 1\times 10^{-3}. \tag{26}$$

Here M_k indicates the number of nodes in the k direction, $\Delta\varphi_{ijk}^N$ is the correction to the field obtained with the ADI method after the marching in the three directions in iteration N, and $\varphi_{\max}^N$ is the maximum value of the field after the iteration N. This convergence criterion was imposed to all variables in the clear fluid and the porous region: vector potential, vorticity vector and temperature. The vector potential interfacial boundary conditions were not imposed directly during the iterative procedure. Therefore, after the convergence criteria given by Eq. (26) were satisfied, it was double checked that the B–J boundary conditions (Eqs. (20)–(22)) were satisfied.

In the following section, the predictions of the model considering the Darcy's law for the momentum transport in the porous medium – described by Eqs. (1)–(6) and (9)–(12) – are compared with the results obtained here with the model that uses Darcy's law with the Brinkman correction factor. For the numerical solution, of this second approach to model the natural convection problem, we used an analogous numerical scheme to the one just described above and proposed by Singh et al. [8]. In our simulations, convective terms were not included in the momentum equations for the porous medium. The convergence criterion given by Eq. (26) was used for the calculation of the two models.

Each one of the results that are presented in this paper was obtained with four different mesh sizes with regular spacing: 11^3, 21^3, 41^3 and 81^3 nodes. A significant difference exists between the temperature and velocity fields obtained with the 11^3, 21^3 and 41^3 node grids. The differences between the fields predicted with 41^3 and 81^3 node grids are negligible. Since the error is augmented by the numerical differentiation needed to obtain the flux at the cold and hot walls, for each given Ra and Da, the convergence analysis was performed by the comparison of the overall Nusselt numbers obtained with the four mesh sizes.

The false transient parameters used in the numerical simulations are given below:

Region	For the potential equations	For the vorticity equations	For the energy equations
Clear fluid	1.0	0.1	5.0
Porous medium	25	No needed	5.0

With these parameters, convergence was obtained for the computer runs that used 11^3, 21^3, 41^3 and 81^3 grid points. However, for the solution with 81^3 grid points of the model that includes the B–J condition, it was necessary to use the parameters 0.5 and 12.5 for the

Table 1
Effect of Rayleigh number, Darcy number and grid size on the overall Nusselt numbers of the hot and cold walls predicted by the solution of the models with Darcy's equation and the model with Darcy's equation plus the Brinkman correction

Grid points	Ra	Brinkman			B–J with $\alpha = 1.0$		
		Hot	Cold	Adopted	Hot	Cold	Adopted
$Da = 10^{-4}$							
11^3	10^4	1.42[a]	1.78		1.1	1.44	
21^3	10^4	1.42[a]	1.60[a]		1.29[a]	1.46[a]	
41^3	10^4	1.42[a]	1.50[a]		1.37[a]	1.45[a]	
81^3	10^4	1.42[a]	1.45[a]		1.41[a]	1.44[a]	
∞	10^4	1.42	1.40	1.42	1.45	1.43	1.44
11^3	10^5	3.62	3.83		2.69	3.24	
21^3	10^5	3.34[a]	3.66[a]		3.10	3.46[a]	
41^3	10^5	3.20[a]	3.35[a]		3.14[a]	3.30[a]	
81^3	10^5	3.17[a]	3.22[a]		3.18[a]	3.23[a]	
∞	10^5	3.10	3.07	3.09	3.22	3.15	3.18
11^3	10^6	6.26	5.45		4.04	4.93	
21^3	10^6	7.45[a]	7.30		6.92	7.05	
41^3	10^6	6.85[a]	7.11[a]		6.79[a]	7.13[a]	
81^3	10^6	6.54[a]	6.67[a]		6.67[a]	6.81[a]	
∞	10^6	6.24	6.23	6.24	6.54	6.49	6.51
$Da = 10^{-3}$							
11^3	10^4	1.51	1.83[a]		1.2	1.51	
21^3	10^4	1.52[a]	1.66[a]		1.39[a]	1.54	
41^3	10^4	1.52[a]	1.57[a]		1.46[a]	1.52[a]	
81^3	10^4	1.52[a]	1.54[a]		1.49[a]	1.52[a]	
∞	10^4	1.52	1.49	1.51	1.52	1.52	1.52
11^3	10^5	4.02	4.10		3.39	3.77	
21^3	10^5	3.81[a]	4.00[a]		3.84	4.11[a]	
41^3	10^5	3.64[a]	3.72[a]		3.91[a]	3.99[a]	
81^3	10^5	3.59[a]	3.62[a]		3.93[a]	3.94[a]	
∞	10^5	3.51	3.48	3.5	3.95	3.87	3.91
11^3	10^6	6.56	6.60		5.94[a]	7.09	
21^3	10^6	8.74	8.73		8.88[a]	10.0	
41^3	10^6	8.48[a]	8.53[a]		10.3[a]	11.1[a]	
81^3	10^6	8.05[a]	8.07[a]		11.1[a]	11.1[a]	
∞	10^6	7.62	7.61	7.62	11.8	11.3	11.5

[a] Indicates the values used in the extrapolation to obtain the values reported in the rows indicated by "∞".

potential equations and the vorticity equations respectively.

Following the work of Singh et al. [8], the false transient parameters were used together with a time step given by $\Delta\tau = \sigma_{st}(\Delta X)^2$. The σ_{st} parameter, which is needed to obtain convergent and stable solutions for all grid sizes, was found to be 2.4. It is possible, that there are another sets of parameters that allow a faster convergence. However, with the set of numerical parameters described above convergence was reached for all grid sizes with any combination of the physical parameters used in the analysis.

4. Results and discussion

To completely define the heat and fluid flow phenomena in the system under study is necessary to fix the parameters: Ra, Pr, Da, L_y/L_x and L_z/L_x. Furthermore, because the cavity contains a two-region structure, it is necessary to define the position of the interface, X_s, the conductivity ratio, K_ω and the parameter, α, when the B–J boundary condition is used.

We have mainly analyzed the effect of Darcy and Rayleigh numbers on the momentum and heat transport, keeping constant the following parameters:

$$Pr = 0.7, \quad L_y/L_x = 1.0, \quad L_z/L_x = 1.0,$$
$$X_s = 0.5, \quad \alpha = 1, \quad K_\omega = 1.$$

Because of the values of the Pr and K_ω parameters, the system is similar to the one found in silos for storing food grains. We have restricted the simulations to $K_\omega = 1$ because Singh et al. [8] demonstrated that variations of order 10 above of this number give similar results in the overall wall Nusselt numbers.

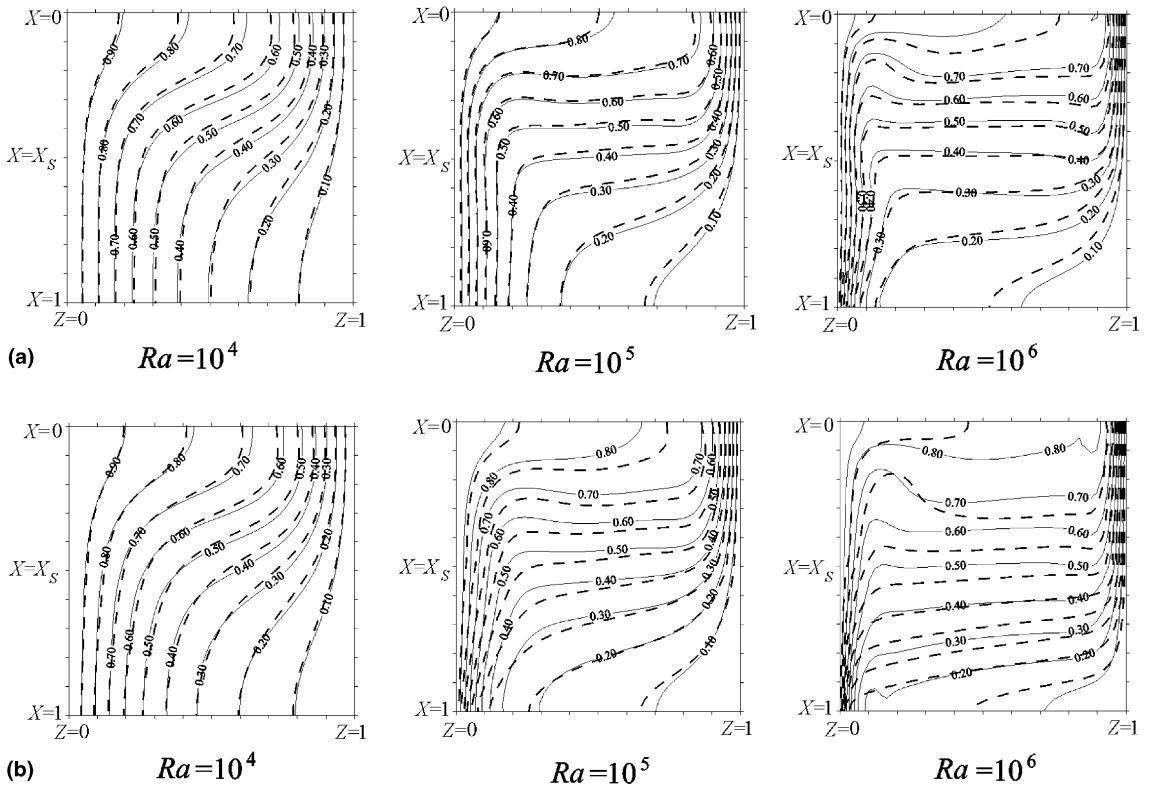

Fig. 2. Effect of Rayleigh number on the isotherms at the plane $Y = 0.5$ for Darcy's numbers: (a) 10^{-4}; (b) 10^{-3}. The continuous lines indicate the predictions by the model without the Brinkman correction term, and the broken lines indicate the prediction by the model with the Brinkman correction term. Other parameters are $\alpha = 1$ and $K_\omega = 1$.

The results reported in this section are for a cubic cavity with half of the volume filled with a porous medium and two of the vertical opposite walls kept at constant temperature: hot wall and cold wall. The zero heat flux boundary condition was imposed in the other four walls.

The predictions resulting from the approach stated in this work, that uses the B–J boundary conditions, are compared with the predictions obtained from the solution of the model that includes the Brinkman correction term in the Darcy's law reported by Singh et al. [8].

As mentioned above the B–J boundary condition parameter was fixed to obtain $\alpha = 1$ for all the results shown lines below. However, previously numerical simulations were obtained with the B–J parameter in the range $0.01 < \alpha < 1$. The results suggest that, for a given situation, there is not a α value that will cause that the B–J approach can yield the same temperature and velocity profiles than the Brinkman extension approach. Therefore all temperature profiles in this work were obtained with $\alpha = 1$.

The convergence of the numerical solution is shown in Table 1 in terms of the overall Nusselt numbers of the hot and cold walls. For each pair of *Ra* and *Da* values, the Nusselt numbers of both walls have a tendency to the value reported in the "adopted" column. The Nusselt numbers that are taken for the comparison between the Darcy's and Brinkman's approaches and to test for the accuracy of the overall heat balance were obtained by a linear extrapolation of the Nusselt number using the inverse of the grid points as the independent variable. As indicated in Table 1, for the extrapolation at $Ra = 10^6$ only the Nusselt numbers predicted from the 41^3 and 81^3 node grids were used. For the other cases reported in Table 1, at least the overall average Nusselt number from the 21^3, 41^3 and 81^3 grids were used for the extrapolation.

We also solved the problem using finer grids close to the isothermal walls: i.e., a 100^3 variable grid mesh with ΔZ next to the walls about 1/3 of the constant spacing corresponding to the 81^3 grid. The comparison of the overall average Nusselt numbers indicates that the difference between the overall average Nusselt number predictions for the situation with $Ra = 10^6$ and $Da = 10^{-3}$ with both type of grids is 3.3%. This difference is much smaller than that obtained between the constant spacing grid predictions from the Darcy's model and the obtained from the model with Darcy–Brinkman extension (49.6%) reported in Table 1. Therefore, the accuracy

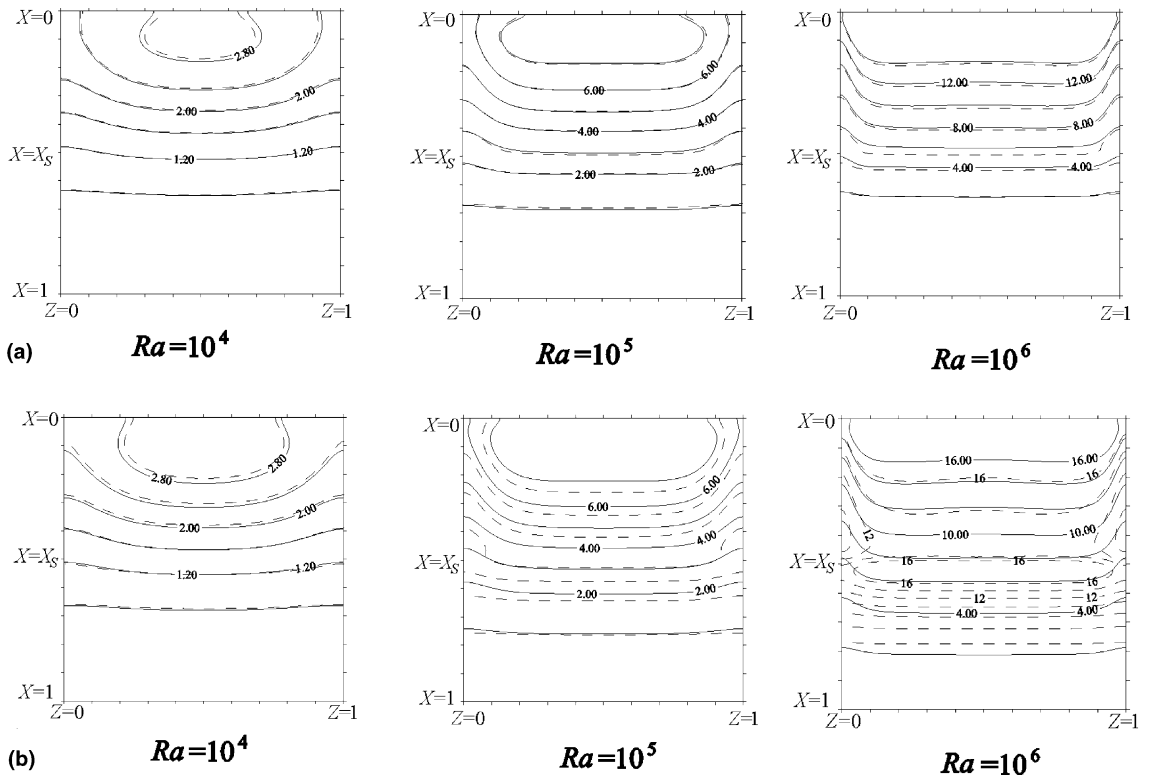

Fig. 3. Effect of Rayleigh number on the local Nusselt at the cold wall ($Y = L_Y/L_X$) for Darcy's numbers: (a) 10^{-4}; (b) 10^{-3}. The continuous lines indicate the predictions by the model without the Brinkman correction term, and the broken lines indicate the prediction by the model with the Brinkman correction term. Other parameters are $\alpha = 1$ and $K_\omega = 1$.

of the results in Table 1 is enough for the purpose of comparing both approaches of modeling the momentum transport in the porous medium region.

The results in Table 1 show that, for every given *Ra* and *Da*, the global heat balance in the system is satisfied within less than 2.2% error. This because the overall Nusselt numbers of the cold and hot wall have a tendency to the same value as the number of nodes is increased.

Because of the temperature boundary conditions at $Y = 0$ and $Y = 1.0$, and the other walls are adiabatic, most of the changes in the temperature and velocity occur in the Y direction and therefore, we report the isotherms in the $Y = 0.5$ plane.

In Fig. 2 the effect of the augment of convection as the Darcy and Rayleigh numbers are increased is shown. In this figure, it is clear that the predicted isotherms from the models with and without the Brinkman correction term are very similar for any of the Rayleigh numbers used, as long the Darcy number is 10^{-4}. In Fig. 2 the differences between the isotherms obtained by the two approaches become larger when *Da* is 10^{-3} and *Ra* is increased. This seems to indicate that viscous effects through the velocity Laplacian of Brinkman correction term is not negligible when the permeability is increased. Most probably, when the permeability becomes big enough the Brinkman formulation is the correct one.

The temperature profiles predicted by the two approaches were used to estimate the hot and cold local Nusselt numbers, as defined by Eq. (25). In Fig. 3 are shown the predicted Nusselt numbers at the cold wall ($Y = 1$) for three Rayleigh numbers and two Darcy numbers. It is clear that, despite the differences shown in Fig. 2 for the isotherms at the vertical plane $Y = 0.5$, both approaches lead to similar results for the local heat transfer rate at the walls. The theoretical predictions of both models confirmed that the Nusselt number in the fluid region is quite independent of variations in the Darcy number, as Singh et al. [8] reported. Although a change is observed, it is possible to say that the Nusselt number in the porous medium region is quite insensitive when the Darcy number changes from 10^{-4} to 10^{-3}.

On the other hand, the results shown in Fig. 3 confirmed that increases in the Rayleigh number significantly augment the Nusselt number.

The changes shown in the contour plots of the local Nusselt number in Fig. 3 are quite monotonic. How-

ever, special attention must be paid at the contour plots corresponding to the predictions from the model that uses the B–J boundary condition for $Ra = 10^6$ and $Da = 10^{-3}$ (right lower corner). For this particular case, around the surface that divides the clear fluid region from the porous region, the B–J model predicts local Nusselt numbers twice the ones predicted by the Brinkman correction model. These differences are better observed in the tri-dimensional plots of the local Nusselt at the cold wall shown in Fig. 4. Here it is clear that B–J model predicts that in the porous medium near X_s, there is a maximum in the Nusselt number. Fig. 4 also shows that the two models predict a maximum for the local Nusselt numbers near the top of the container.

The presence of a maximum in the maps of Nusselt numbers is better observed in Fig. 5. Here we have plotted the width average Nusselt number $\overline{Nu}_X(X)$, as defined by Eq. (24a), for the hot and cold walls as function of the vertical position. In Fig. 5(a), it can be seen that for $Da = 10^{-4}$ the differences between the heat transfer rate predicted by the two approaches could be neglected except at the hot wall for $Ra = 10^6$.

In Fig. 5(b) it is obvious that the differences between the width average Nusselt predicted by the two considered approaches become larger as the Rayleigh and Darcy numbers are augmented. The largest differences were found for $Ra = 10^6$ and $Da = 10^{-3}$.

Also, the results in Fig. 5(b) show that, in most cases, both models predict that the largest effects of the convection are in the bottom of the hot wall and in the top of the cold wall. However, when $Ra = 10^6$ the heat transfer rate normal to the cold wall near the interface is pretty close to the one near the top of the container. As shown in Table 1, the global heat balance is satisfied with less than 2.5% of error despite the big differences between the profiles of the width Nusselt number of the cold and hot walls.

In Table 2 a comparison of the overall average Nusselt numbers obtained from the three-dimensional problem with those obtained from the two-dimensional problem is shown. The same type of convergence analysis was performed for the two-dimensional predictions. The comparison shows that the two-dimensional Nusselt numbers are always bigger than the three-dimensional predictions as mentioned by Singh et al. [8].

Therefore, there is reason to accept that the two approaches lead to important differences in the prediction of the global heat transfer effects when the Raleigh and Darcy numbers are 10^6 and 10^{-3}, respectively. Most probably this difference will become larger if the Da and Ra are augmented.

All results shown in the previous figures did not take into consideration inertial effects in the porous medium. In Fig. 6 we compare the temperature and Ψ_Z contour plots at $Y = 0.5$ predicted by the two models when inertial effects are included. The comparison of the upper plots with the lower plots in Fig. 6 shows that the predictions by the model with the Brinkman's correction are less affected by the inclusion of the inertial terms. These results suggest the effect that the addition of the convective terms in the momentum transport equation of the porous medium will have a significant effect on the heat transfer rate. Therefore, a systematic study of the convective effects must be carried out. However, one must remember that if the convective terms are added to the momentum equation, it may be necessary to add other terms to the interfacial boundary condition [12,18].

5. Conclusions

We presented a comparison of two models to study heat transport by buoyancy-driven flow in a fluid/porous medium system contained in a cavity. In the first approach, the momentum transport was modeled in terms of the Navier–Stokes and Darcy's law equation. An extension of the B–J semi-empirical boundary condition was used to couple the momentum equations of the clear

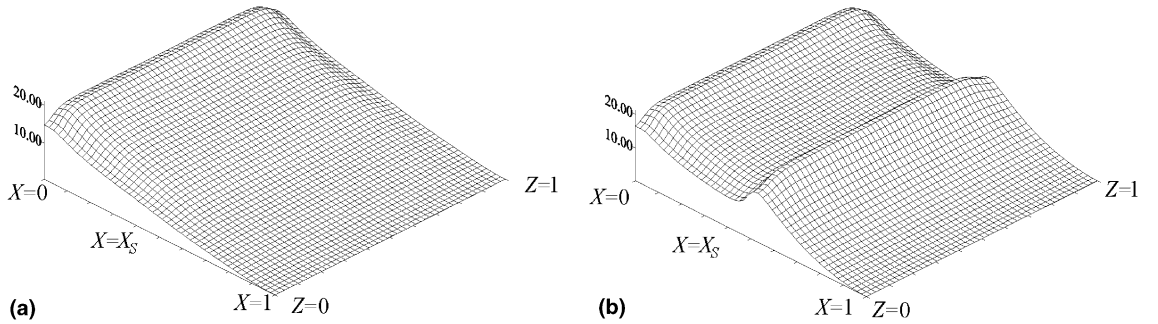

Fig. 4. Comparison of the local Nusselt number at the cold wall predicted by: (a) the model with the Brinkman correction term; (b) the model without the Brinkman correction term. The parameters are $Ra = 10^6$, $Da = 10^{-3}$, $\alpha = 1$ and $K_\omega = 1$.

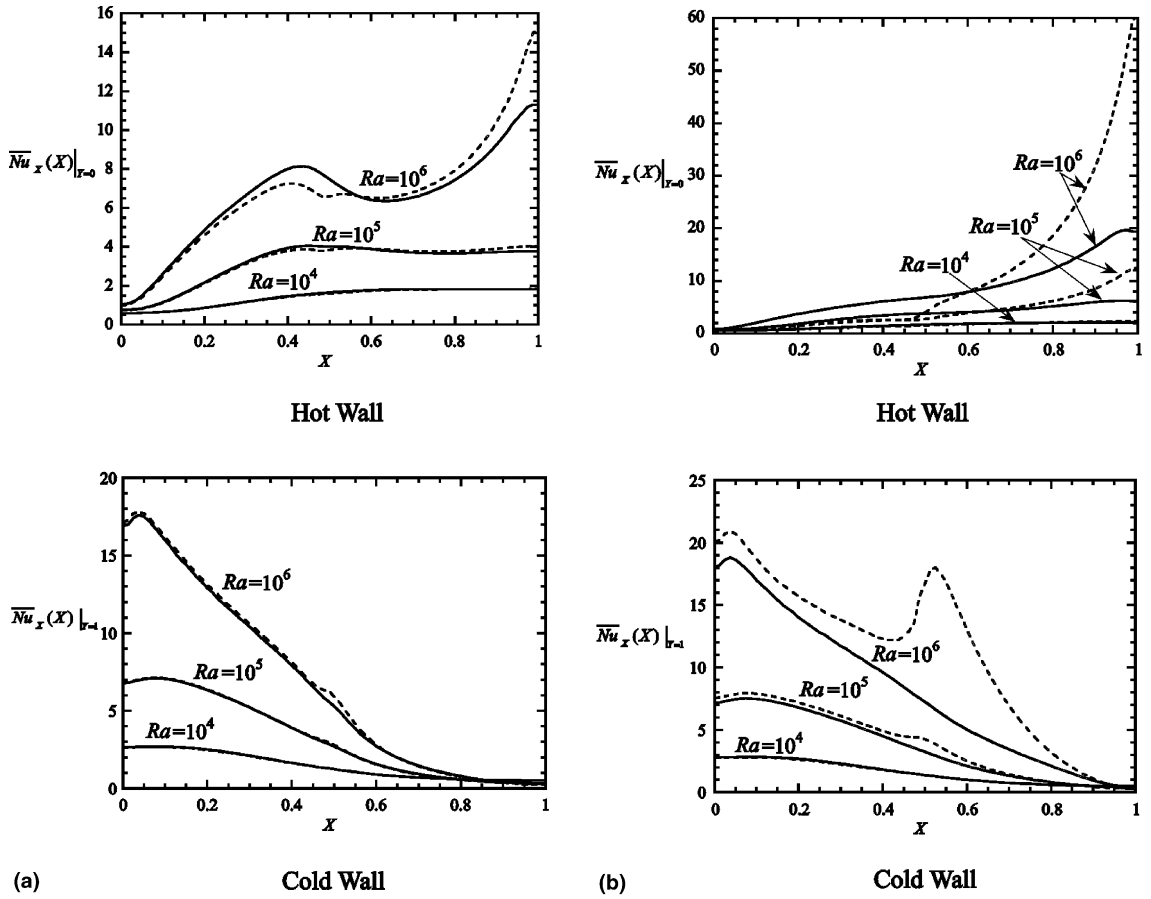

Fig. 5. Effect of Rayleigh number on the width average Nusselt number $\overline{Nu}_X(X)$ at the hot and cold walls. (a) $Da = 10^{-4}$; (b) $Da = 10^{-3}$. The continuous lines indicate the predictions by the model without the Brinkman correction term, and the broken lines indicate the prediction by the model with the Brinkman correction term. Other parameters are $\alpha = 1$ and $K_\omega = 1$.

Table 2
Comparison of the overall Nusselt numbers of the system predicted by the solution of the tri-dimensional (3-D) and two-dimensional (2-D) models with Darcy's equation and the model with Darcy's equation plus the Brinkman correction

Ra	*Da*	Brinkman		B–J with $\alpha = 1.0$	
		3-D	2-D	3-D	2-D
10^4	10^{-4}	1.41	1.52	1.44	1.56
10^4	10^{-3}	1.51	1.63	1.52	1.62
10^5	10^{-4}	3.09	3.26	3.18	3.39
10^5	10^{-3}	3.5	3.69	3.91	4.10
10^6	10^{-4}	6.24	6.35	6.51	6.83
10^6	10^{-3}	7.62	7.78	11.5	11.4

fluid and porous medium regions. The second approach considers Darcy's law with Brinkman's correction term. In this case, continuity of velocity and stress were used as the interfacial boundary conditions.

The numerical solution that involved the finite difference representation with an ADI scheme was obtained in terms of the vorticity-vector potential formulation.

The differences between the temperature and velocity contour plots predicted by the two approaches increase as the intensity of the fluid motion and the permeability of the porous media are augmented. From a practical point of view, the difference between the predictions of the two models becomes significant when the heat transfer rates at the walls of the container are compared in the parametric region given by $Ra \geqslant 10^5$ and $Da \geqslant 10^{-3}$.

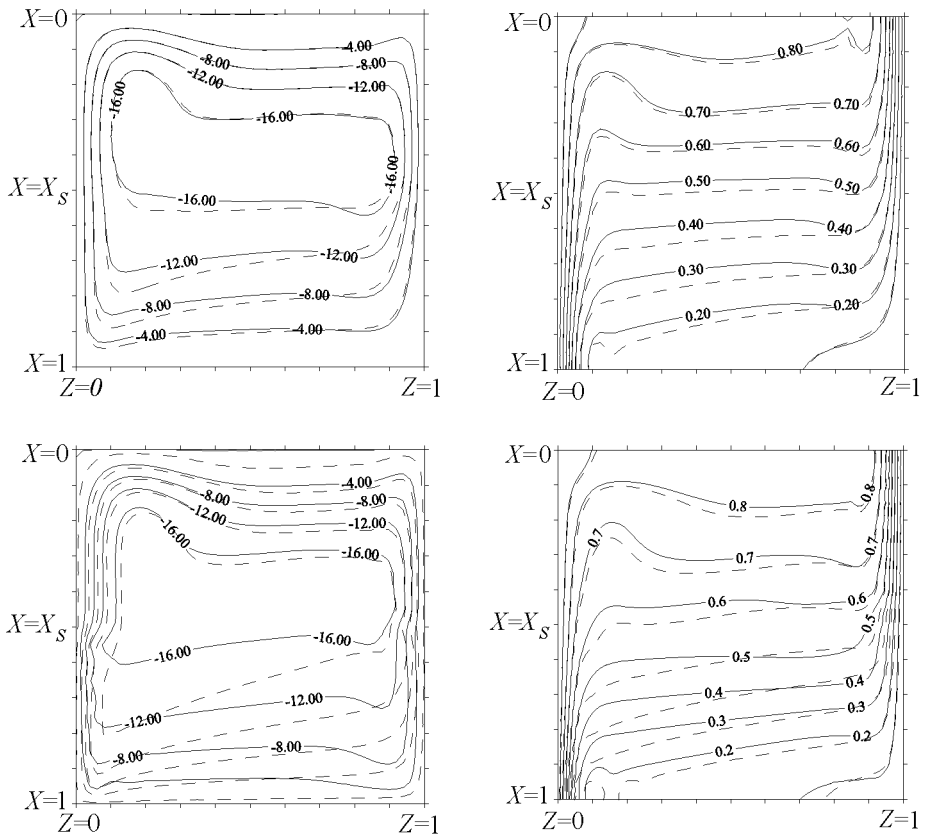

Fig. 6. Comparison of potential Ψ_Z and isotherms predicted at $Y = 0.5$ when convective terms are included in the models (continuous lines) and without convective effects (broken lines). The upper figure data were obtained using the model with Brinkman correction term. The lower figure data were obtained using the model without Brinkman correction term. The parameters are $Da = 10^{-3}$, $Ra = 10^6$, $\alpha = 1$ and $K_\omega = 1$.

This indicates the necessity of experimental work to clarify which is the correct form of modeling the momentum transport in porous media. The experimental work should be oriented to obtain local average velocity and temperature measurements. A more systematic study that involves the simulation with the two approaches should be used to decide where to take the measurements.

Acknowledgements

The authors wish to thank the Consejo Nacional de Ciencia y Tecnología (CONACyT) and the Instituto Mexicano del Petróleo (IMP) for financial support.

References

[1] S. Whitaker, Local thermal equilibrium: an application to packed bed catalytic reactor design, Chem. Eng. Sci. 41 (1986) 2029–2039.

[2] D. Poulikakos, A. Bejan, B. Selimos, K.R. Blake, High Rayleigh number convection in a fluid overlaying a porous bed, Int. J. Heat Fluid Flow 7 (1986) 109–116.

[3] F. Chen, C.F. Chen, Onset of finger convection in a horizontal porous layer underlying a fluid layer, ASME J. Heat Transfer 110 (1988) 403–409.

[4] T. Nishimura, T. Takumi, M. Shiraishi, Y. Kawamura, H. Ozoe, Numerical analysis of natural convection in a rectangular enclosure horizontally divided into fluid and porous regions, Int. J. Heat Mass Transfer 29 (1986) 889–898.

[5] C. Beckerman, S. Ramadhyani, R. Viskanta, Natural convection flow and heat transfer between a fluid layer and a porous layer inside a rectangular enclosure, ASME J. Heat Transfer 109 (1987) 363–370.

[6] C. Beckerman, R. Viskanta, S. Ramadhyani, Natural covection in vertical enclosures containing simultaneously fluid and porous layers, J. Fluid Mech. 186 (1988) 257–286.

[7] S.B. Sathe, W.Q. Tong, T.W. Tong, Natural convection in enclosures containing and insulation with a permeable fluid–porous interface, Int. J. Heat Fluid Flow 9 (4) (1988) 389–395.

[8] A.K. Singh, E. Leonardi, G.R. Thorpe, Three-dimensional natural convection in a confined fluid overlaying a porous layer, ASME J. Heat Transfer 115 (1993) 631–638.

[9] H.C. Brinkman, A calculation of the viscous force exerted by a flowing fluid on a dense swarm of particles, Appl. Sci. Res. A 1 (1947) 27–34.
[10] J.A. Ochoa-Tapia, S. Whitaker, Momentum transfer at the boundary between a porous medium and a homogeneous fluid – I. Theoretical development, Int. J. Heat Mass Transfer 38 (1995) 2635–2646.
[11] G. Beavers, D.D. Joseph, Boundary conditions at a naturally permeable wall, J. Fluid Mech. 30 (1967) 197–207.
[12] S. Whitaker, The Forchheimer equation: a theoretical development, Transport Porous Media 25 (1996) 27–61.
[13] S. Whitaker, Flow in porous media I: a theoretical derivation of Darcy's law, Transport Porous Media 1 (1986) 3–25.
[14] G. Mallinson, G. de Vahl Davis, Three-dimensional natural convection in a box: a numerical study, J. Fluid Mech. 83 (1977) 1–31.
[15] F. Stella, G. Guj, E. Leonardi, G. de Vahl Davis, The velocity/vorticity and vector potential/vorticity formulations, three-dimensional natural convection, in: Proceedings of the Third Italian Conference of Computational Mechanics (AIMETA), 1988.
[16] G. Mallinson, G. de Vahl Davis, The method of false transient for the solution of coupled elliptic equations, J. Comput. Phys. 12 (1973) 435–461.
[17] D.W. Peaceman, D.D. Rachford, The numerical solutions of parabolic and elliptic differential equations, Soc. Ind. Appl. Math. J. 3 (1955) 28–47.
[18] J.A. Ochoa-Tapia, S. Whitaker, Momentum jump condition at the boundary between a porous medium and a homogeneous fluid: inertial effects, J. Porous Media 1 (1998) 201–217.